

UC Riverside

UC Riverside Electronic Theses and Dissertations

Title

The Effect of Processing Parameters on the Thermoelectric Properties of Magnesium Silicide

Permalink

<https://escholarship.org/uc/item/6dp2z8nj>

Author

Fong, Anthony

Publication Date

2012

Peer reviewed|Thesis/dissertation

UNIVERSITY OF CALIFORNIA
RIVERSIDE

The Effect of Processing Parameters on the Thermoelectric
Properties of Magnesium Silicide

A Thesis submitted in partial satisfaction
of the requirements for the degree of

Master of Science

in

Mechanical Engineering

by

Anthony Yun-Ming Fong

September 2012

Thesis Committee:

Dr. Javier Garay, Chairperson

Dr. Christopher Dames

Dr. Lorenzo Mangolini

Copyright by
Anthony Yun-Ming Fong
2012

The Thesis of Anthony Yun-Ming Fong is approved:

Committee Chairperson

University of California, Riverside

Acknowledgements

I would like to dedicate this work to my family and friends for their help and support.

ABSTRACT OF THE THESIS

The Effect of Processing Parameters on the Thermoelectric Properties of Magnesium Silicide

by

Anthony Yun-Ming Fong

Master of Science, Graduate Program in Mechanical Engineering
University of California, Riverside, September 2012
Dr. Javier Garay, Chairperson

Thermoelectric materials are unique in their ability to directly convert thermal energy into electrical. Various applications include: energy scavenging, spot cooling and heating, and interstellar power generation. Current research is geared towards improving thermoelectric materials for greater energy conversion efficiency. Mg_2Si has been a good candidate for study due to its low toxicity, low density, and availability of constituent elements. Recent efforts to improve efficiency of bulk thermoelectric materials have included, but are not limited to, changing the electronic band structure through doping or altering the microstructure. While the former has been well studied and verified, the latter remains relatively untouched experimentally. There is evidence that thermoelectric materials with low dimensionality show improvement in certain properties. Thin films and nanowires are known to have lower thermal conductivities than their bulk counterparts. The goal of this work is to provide evidence of microstructural effects on the thermoelectric properties of bulk Mg_2Si .

The three relevant properties for thermoelectric materials are thermal conductivity, electrical conductivity, and the Seebeck coefficient. Because commercial measurement systems are costly and have limited measurement ranges and accuracies, the development of custom equipment is sometimes necessary. An electrical AC current source is developed

and used to measure the electrical conductivity and, through the 3ω method, thermal conductivity of bulk samples. The measured values are comparable, with a 3% agreement, to a separate well-established system.

The bulk samples are consolidated from powder using the Current Activated Pressure Assisted Densification (CAPAD) process. It is known that different processing temperatures alter the amount of grain growth during the densification process. Samples processed at higher temperatures show increasing thermal and electrical conductivities while the Seebeck coefficient decreases. These trends lead to a maximum figure of merit value with the sample processed at an intermediate temperature.

Table of Contents

List of Figures	viii
List of Tables.....	x
Chapter 1 Introduction.....	1
1.1 Motivation	1
1.2 Introduction to Thermoelectric Materials	1
1.3 Review of the State of the Art.....	3
1.4 Metrology.....	4
1.5 Current Activated Pressure Assisted Densification (CAPAD).....	6
Chapter 2 Development of Metrology Equipment	9
2.1 Introduction.....	9
2.2 Circuit Design and Theory	10
2.3 Results.....	16
2.4 Discussion.....	19
2.5 Conclusions	20
Chapter 3 Synthesis, Characterization, and Property Measurement of Magnesium Silicide .	21
3.1 Introduction.....	21
3.2 Experimental Procedures	21
3.2.1 Powder Processing.....	21
3.2.2 CAPAD	22
3.2.3 Microstructure Analysis.....	24
3.2.4 Property Measurements	25
3.3 Results.....	27
3.4 Discussion.....	36
3.5 Conclusions	37
References	38

List of Figures

Figure 1.1: Crystal structure of Magnesium Silicide. Silicon atoms are in the face centered positions while the Magnesium atoms are in the tetrahedral positions.	3
Figure 1.2: Cross sectional view of the CAPAD apparatus. Points of interest are labeled.....	8
Figure 2.1: Schematic of an inverting operational amplifier circuit with resistors R1 and R2.	11
Figure 2.2: Diagram of an inverting op amp circuit with the current path outlined in red. ...	11
Figure 2.3: Two stage amplifier circuit. The first stage amplifies the signal from a voltage source while the second stage maintains a constant current through the sample R4.....	12
Figure 2.4: Picture of the circuit on a prototyping breadboard. The two integrated circuit amplifiers (ICs) are shown in the center. Resistors and capacitors are labeled.	13
Figure 2.5: Simplified current source circuit with instrumentation amplifiers. The lock in, computer and DAC form a feedback loop to match the voltage drop across R3 and R4 read by the computer.	14
Figure 2.6: A complete 3ω circuit diagram with components and connections labeled. IC datasheets were consulted for wiring and application instruction.....	15
Figure 2.7: Basic layout of sample stage and heat sink relative to the thermoelectric module.	16
Figure 2.8: Current source voltage output error for a range of voltages and frequencies. Maximum error is 0.47% at 100 Hz with input voltage amplitude of 0.75V. There is no apparent relationship between accuracy, frequency, or input voltage.....	17
Figure 2.9: 3rd harmonic voltage output by the current source. There is an increasing trend with increasing input voltage.	18
Figure 2.10: Thermal conductivity of AlN and Al ₂ O ₃ vs Temperature. Solid shapes represent the values from the equipment built in this thesis. Outlined shapes represent the values from the previously established system.	19
Figure 3.1: Cross section of mini die within a regular sized graphite die and plunger set.	23

Figure 3.2: Sample CAPAD temperature and pressure curves during an experiment. The experiment lasted 400 seconds using a pressure of 112 MPa and temperature of 775 °C. ...	24
Figure 3.3: Evolution of the (220) XRD peak under different ball milling conditions. The peak shift in 2θ can be attributed towards either a change in lattice parameters or sample alignment in the instrument.	28
Figure 3.4: a) SEM micrograph (secondary electron) of Mg ₂ Si powder as received b) SEM micrograph of Mg ₂ Si powder ball milled at 600 RPM for 48 hours. Note the wide dispersion of particulate size.....	29
Figure 3.5: Relative densities of samples processed at varying temperatures. Regardless of hold time, a maximum density is reached for samples above 650 °C. Two samples were processed at 650 °C with densities at 99% of theoretical maximum.....	29
Figure 3.6: Relative densities from varying processing temperatures disregarding hold time. Four separately prepared powders were used. All powders reach their maximum density with processing temperatures above 675 °C.	30
Figure 3.7: XRD curves of the ball milled powder (600RPM, 48hr) and densified samples...	32
Figure 3.8: SEM micrograph (secondary electron) of the polished surface of the sample processed at 850 °C. Grains can be seen on the order of 50 nm.	33
Figure 3.9: a) Electrical conductivities of samples processed at different temperatures. Higher processing temperatures result in a greater electrical conductivity. Less extensive ball milling also results in greater electrical conductivities. b) Seebeck coefficients c) Thermal conductivities and d) ZT of samples processed at different temperatures.	34

List of Tables

Table 2.1: Current source main components list.....	16
Table 3.1: Estimated grain size from the Scherrer equation neglecting contributions from the instrument.	27
Table 3.2: Processing parameters and corresponding densities.	30
Table 3.3: Processing parameters and densities.	31
Table 3.4: Thermoelectric properties and estimated grain sizes (XRD) of samples.....	33
Table 3.5: Comparison of total thermal conductivity and the electron contribution.....	36

Chapter 1 Introduction

1.1 Motivation

Thermoelectric materials are currently a major interest for their potential applications towards renewable energy sources and energy scavenging. It is well known that the microstructure of materials and devices greatly affect their properties [1–8]. Micro and nanometer grain sizes interfere with the movement of energy carriers due to the increased number of grain boundaries present. The three key properties for a thermoelectric material are: thermal conductivity, electrical conductivity, and its Seebeck coefficient. Studies on other material systems such as Silicon-Germanium, Bismuth-Telluride, etc, have shown decreases in thermal and electrical conductivity.

This thesis is organized into three parts: Chapter 1 is a general introduction to thermoelectric properties, measurement, and processing techniques. Chapter 2 documents the development, construction, and implementation of a thermal and electrical conductivity measurement system. Chapter 3 details the synthesis and characterization of bulk thermoelectric (TE) samples. Samples of Magnesium Silicide, Mg_2Si , were synthesized to elucidate the role of microstructure on the TE properties.

1.2 Introduction to Thermoelectric Materials

There are three major phenomena that govern thermoelectric materials: the Seebeck, Peltier, and Thomson effects. The study of thermoelectric materials began with the discovery of the Seebeck effect named after Thomas Seebeck who discovered the

phenomenon in 1821 [9]. Seebeck found when two dissimilar metals are joined together and the junctions are held at different temperatures an electrical current and voltage is produced proportional to the temperature difference. The original experiment deflected a compass needle and the phenomenon was named the thermomagnetic effect. Upon further investigation, it was later found that the magnetic field was generated by the induced current. This voltage difference is due to the intrinsic property of the material referred to as the Seebeck effect. A second effect of thermoelectrics is called the Peltier effect named after Jean Peltier, where an induced electrical current causes a temperature difference [10]. The third and final effect is the Thomson effect named after William Thomson or Lord Kelvin, where heat is absorbed or rejected when current flows through a thermoelectric material under a temperature gradient [11].

Thermoelectric materials are characterized by the dimensionless figure of merit: ZT , which relates to the conversion efficiency between thermal and electrical energy. ZT is the relationship between the electrical, thermal, and Seebeck properties of a material multiplied by temperature. Calculation of ZT is as follows:

$$ZT = \frac{S^2 \sigma}{\kappa} T \quad 1.1$$

where S is the Seebeck coefficient [V/K], σ is the electrical conductivity [S/m], κ is the thermal conductivity [W/m·K], and T is the absolute temperature [K]. From a first approximation, higher ZT values can be obtained simply through higher operating temperatures. All these three properties are connected such that changing any one of the properties affects the other two. The forefront of research in thermoelectric materials has been focused on improving the figure of merit, ZT . The two most popular methods for

achieving this are altering the amount of charge carriers and mobility of energy carriers (electrons and phonons). Semiconducting materials generally have large Seebeck coefficients with values in the hundreds of microvolts per Kelvin whereas metals are orders of magnitude less.

The major material system discussed in this thesis is magnesium silicide, Mg_2Si . Mg_2Si has been an excellent candidate for thermoelectric material study. Its low density of 2 g/cm^3 is nearly a fourth of bismuth telluride (a popular TE material used for many commercial applications) and on par with silicon. It is also non-toxic compared to other materials which contain lead and antimony. The abundance and availability of silicon and magnesium also makes Mg_2Si a candidate for production in large quantities. Mg_2Si forms in the anti-fluorite structure with the silicon atoms at the face center cubic positions and the magnesium atoms at the tetrahedral positions as shown in Figure 1.1.

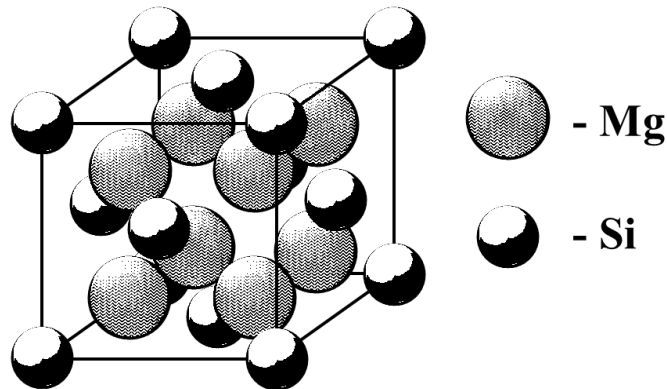


Figure 1.1: Crystal structure of Magnesium Silicide. Silicon atoms are in the face centered positions while the Magnesium atoms are in the tetrahedral positions.

1.3 Review of the State of the Art

Major research efforts into the field of thermoelectric materials exploded in the 1950s and continued on into the 1960s [12]. Thermoelectric generators, refrigerators, and portable biological specimen holders were prototyped during this time [13]. There was a loss in interest during the 1970s when it was theorized that the maximum figure of merit achievable was approximately $ZT \sim 1$. Resurgence in interest of thermoelectric materials arose with the advance in materials science in the micro and nanometer scale [7].

Current cutting edge thermoelectric research makes use of exotic materials and unique structures to fine tune the properties. Thin films and nanowires have always been of interest due to their low dimensionality and improved properties. These structures approach the length scales of the energy carriers and drastically change the overall interactions between carrier and structure. A ZT of ~ 1.6 at room temperature has been reported using quantum dot superlattices of PbSeTe/PbTe [14]. Dr. Venkatasubramanian and group has also been successful in creating a thin film superlattice of Bi₂Te₃/Sb₂Te₃ with $ZT \sim 2.4$ at room temperature [15].

1.4 Metrology

The measurement process of materials can often be difficult and expensive. Precautions must be taken in order to ensure accuracy. It is often necessary to develop and build custom systems in order to provide accurate measurements.

Of all the methods to measure electrical conductivity, the technique known as the four probe method is the most popular. There are many variations for this method, but the underlying principle is the same. Only two instruments are needed: an electrical current

source that will produce a known current and a voltage meter. The idea behind this is to use Ohms law where the voltage drop between two points on the sample is proportional to the product of the resistance and amount of current flowing through the circuit, $V=IR$. Many benchtop multimeters have this functionality built in as well as the less accurate two wire method. Using four wires is ideal because the probe and contact resistance are greatly mitigated in the final measurement value compared to the two wire method. Semiconductor electrical resistivity measurement can be tricky due to having either Ohmic or Schottky contacts. Schottky contacts are a product of metal-semiconductor junctions and display rectifying characteristics. Ohmic contacts produce a linear response.

Thermal conductivity of bulk samples is often measured via the thermal flash method. The concept behind the thermal flash method is to have an isotropic bulk sample of known shape and instantaneously heat one side while measuring the temperature response on the opposing side. The temperature rise time is a measure of thermal diffusivity and from the diffusivity, thermal conductivity can be calculated using the relationship: $\kappa = \alpha\rho C$, where κ is the thermal conductivity, α is the thermal diffusivity, ρ is the density, and C is the specific heat of the sample.

Another popular method is the 3ω method made popular by Cahill [16]. The 3ω method is a frequency variation of the hot wire method where a thin heater of known properties and dimensions is microfabricated to the surface of a sample and based on the amount of power dissipated and temperature change, the thermal conductivity of the sample can be calculated. Time domain thermal reflectance is a recently modified optical method for measuring thermal conductivity [17]. This technique relies on the change in reflectance of the surface of a sample upon heating.

Measurement of a sample's Seebeck coefficient is fairly straightforward. Tritt describes a setup in which a heater, heat sink, thermocouples, and voltage leads are attached to a sample [18]. While the Seebeck coefficient is not dependent on the geometry of isotropic samples; thermocouple and voltage lead placements are crucial. Requirements for good measurements include: identical placement (spatial and temporal) of temperature and voltage probes, good thermal and electrical contacts, and high sensitivity voltage measurements [19].

1.5 Current Activated Pressure Assisted Densification (CAPAD)

A useful method for creating bulk samples from powder with unique properties is the current activated pressure assisted densification (CAPAD). This method is frequently called spark plasma sintering. Due to its precision heating and pressure loading control, the microstructure of the bulk sample can be tuned depending on the processing parameters. A schematic of the cross sectional setup of the CAPAD device is illustrated in Figure 1.2

The densification process of powders takes place through a combination of particle rearrangement, fracture, yield, and sintering [20], [21]. The first three are primarily caused by the applied external pressure compacting the powder. All three (particle rearrangement, fracture, and yield) can be highly temperature dependent. Sintering is driven by the reduction in the free surface energy of the powder compact. Two ways this can happen is through the coarsening of particles and densification. Particle coarsening is basically the coalescing of small particles into a fewer larger particles. Densification is the reduction of voids between particles. Sintering is generally described to have three phases: initial,

intermediate and final. During the initial stage of sintering, two adjacent particles neck together. The intermediate phase consists of networks of connected polyhedra and pores as the particles move closer towards each other. The final stage results in the isolation and shrinkage of the pores as a result of densification.

Grain growth occurs when a polycrystalline material is brought to an elevated temperature [22]. The driving force behind grain growth is the same as sintering: to reduce the amount of free surface energy. Normal grain growth constitutes the average size of grains growing larger. Abnormal grain growth is an inhomogeneous growth of grains where some may grow larger than the surrounding grains. Coarsening, sometimes referred to as Ostwald ripening, is the evaporation of small grains and condensation on larger grains. Impurities and anisotropy also affect grain growth by introducing other secondary factors such as interfaces, diffusion coefficients, and grain boundary mobility. It is generally accepted that the amount of normal grain growth in a material follows the relationship [23]:

$$r^m = r_0^m + \alpha_0 t (e^{\frac{-Q}{kT}}) \quad 1.2$$

where r is the average grain radius after a time t , r_0 is the initial average radius, α_0 is a constant, Q is the activation energy, k is Boltzmann's constant, T is the temperature, and m is a fitting parameter. The expected value of m is 2, but higher values are sometimes found. This equation states that grain growth is exponentially driven by the temperature of the material; the amount of time spent at a temperature results in a linear relationship.

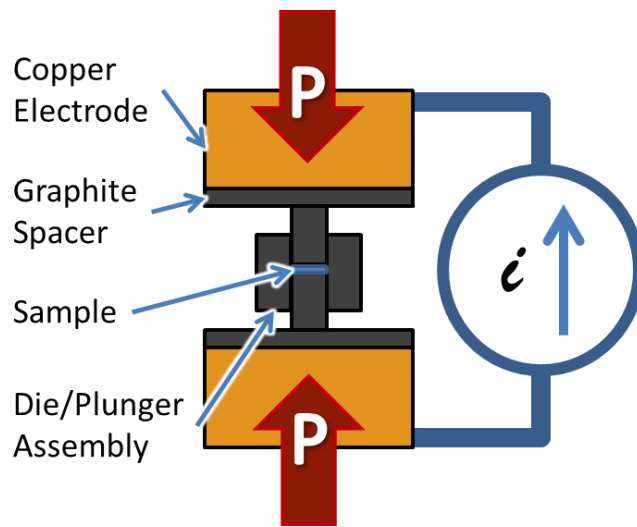


Figure 1.2: Cross sectional view of the CAPAD apparatus. Points of interest are labeled.

Chapter 2 Development of Metrology Equipment

2.1 Introduction

Property measurement, metrology, of materials is an integral part of materials science. Entire labs and companies are founded for the sole purpose of precision measurements. These measurements are made possible through high precision electrical equipment. Power supplies, voltage sources, multimeters, and oscilloscopes are among the most basic and popular instruments used. A current source acts very similarly to a voltage source with one key difference: a current source outputs a constant current value while a voltage source outputs a set voltage. This section documents the development of a measurement system for the thermal conductivity of bulk samples through the 3ω method.

The 3ω experiment is an AC measurement technique for determining the thermal conductivity of materials. This type of experiment uses a metal line heater/thermometer that is microfabricated on the surface of the sample. A sinusoidal current through the heater at frequency 1ω heats the sample at 2ω . This temperature fluctuation caused by heating at 2ω also changes the resistance of the heater. The resistance change at 2ω and current at 1ω produces a voltage at 3ω . This 3ω voltage is measured by a lock in amplifier at two different frequencies f_1 and f_2 to calculate the thermal conductivity k :

$$k = \frac{V^3 \ln \frac{f_2}{f_1}}{4\pi l R^2 (V_{3,1} - V_{3,2})} \frac{dR}{dT} \quad 2.1$$

The current source circuit was created because there was a high demand for 3ω experiments such that the existing setup was in constant queue. The existing setup included a Janis cryostat, Stanford Research Systems SR830 lock-in amplifier, and Keithley 6221 AC

current source. An additional AC current source was needed in order to create a second 3ω measuring station. However another Keithley 6221 AC current source was not available. The Keithley 6221 also has the limitation of 100mA maximum current output. Creating a custom current source circuit would allow the opportunity for a higher output. This circuit is also paired with a voltage subtraction circuit that feeds into the lock in amplifier in order to more easily detect the third harmonic signal [16].

2.2 Circuit Design and Theory

An amplifier based circuit was utilized to create the AC current source due to its well understood theory, low cost, and wide variation of models. An operational amplifier circuit is a natural current source. The current flowing through the feedback loop resistor is ideally constant. There are two ways to visualize this. The first way is to take a look at the inverting op amp circuit in Figure 2.1. The gain of the circuit is: $G = -\frac{R2}{R1}$ such that $V_{out} = V_{in} * G$. Where V is the voltage potential and R1 and R2 are resistors 1 and 2. The output voltage, at node 3, of the op amp is the ratio of the feedback resistor, R2, and the input resistor, R1, times the input voltage. If resistor R2 was to change value, V_{out} at node 3 would change by the same ratio. Using Ohm's law and understanding the ideal op amp model where the voltage at node 2 is equal to zero or ground voltage, the voltage and resistance ratios never change. If R2 doubles, so does V_{out} .

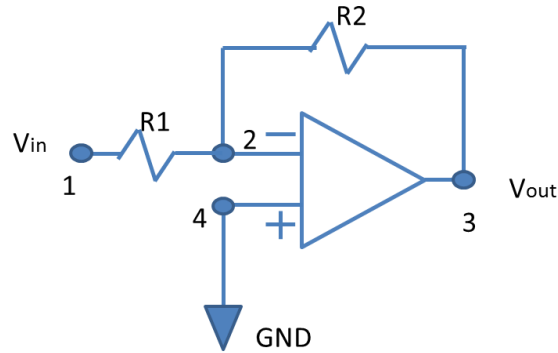


Figure 2.1: Schematic of an inverting operational amplifier circuit with resistors R1 and R2.

Another way of analyzing an op amp circuit as a constant current source is by taking a look at the resistor R1. The ideal op amp model states that node 2 is linked together with node 4 which is connected to ground. There is no voltage difference between the two nodes so there is no current flowing through that path. The only path for current is through nodes 1, 2, and 3 which span across the resistors R1 and R2 as shown in Figure 2. The amount of current flowing through the feedback resistor is only dependent on the first resistor, R1

$$I = \frac{V}{R1} \quad 2.2$$

where I is the amount of current flowing through the resistor in Amperes.

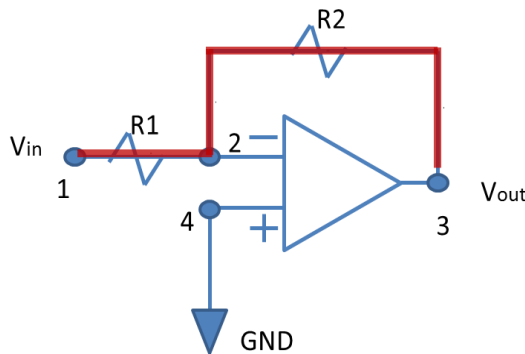


Figure 2.2: Diagram of an inverting op amp circuit with the current path outlined in red.

The final current source uses two stages of operational amplifier circuits shown in Figure 2.3. A complete list of main electronic components with part numbers and descriptions can be found in Table 2.1. The design uses two amplifiers to produce a constant current across resistors R3 and R4. R4 represents the resistance of the 3ω sample heater. R3 is a high precision and high power resistor selected to handle the amount of current. There are two op amps in the circuit to minimize the amount of power load on the function generator. A 50Ω precision resistor is the chosen value for R1. R2 is a 500Ω precision resistor making the gain of the first stage -10. The amount of current flowing through the 3ω sample heater is expressed by the equation:

$$I = V_{in} \frac{R2}{R1 \cdot R3} \quad 2.3$$

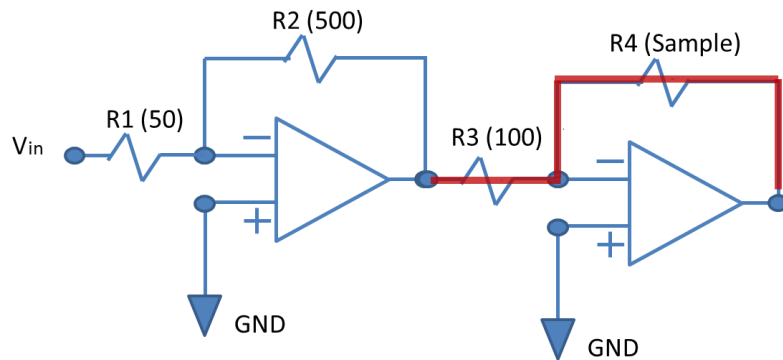


Figure 2.3: Two stage amplifier circuit. The first stage amplifies the signal from a voltage source while the second stage maintains a constant current through the sample R4.

The 50Ω resistor was chosen in order to make the circuit into a 50Ω terminated circuit to minimize the amount of signal reflection and power loss through the wires[24]. Many voltage signal generators have an internal 50Ω resistor that is used to calculate the output voltage.

Additional precautions are taken to reduce the amount of unwanted noise from the circuit. $10\mu\text{F}$ capacitors are connected across the both $\pm 15\text{V}$ power supply rails directly to ground. $0.1\mu\text{F}$ capacitors are also shunted across the $\pm 15\text{V}$ power supply rails as close to the op amps as physically possible. The spatial placement of the capacitors is necessary to discourage any amount of crosstalk and noise from external sources. The capacitors in this configuration are commonly called bypass capacitors [25].

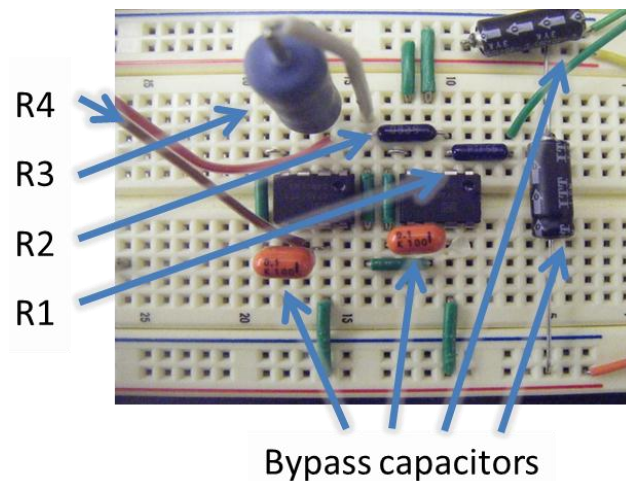


Figure 2.4: Picture of the circuit on a prototyping breadboard. The two integrated circuit amplifiers (ICs) are shown in the center. Resistors and capacitors are labeled.

The 3ω voltage is typically $1000\times$ smaller in amplitude than the 1ω voltage. This presents a problem because it approaches the limit that most lock in amplifiers can resolve a signal. The solution is to use the lock in amplifier in differential mode. A precision resistor is placed in series with the sample's line heater. The voltage drop across each individual resistor is read by the lock in's channel A and B. When in differential mode, the lock in displays the difference between the two voltages at A and B. If the amplitude of A and B are the same at the 1ω frequency, the resulting voltage is zero. Assuming that no 3ω noise is

generated by the series resistor, this will leave only the 3ω signal produced by the sample line heater and is easily read by the lock in amplifier.

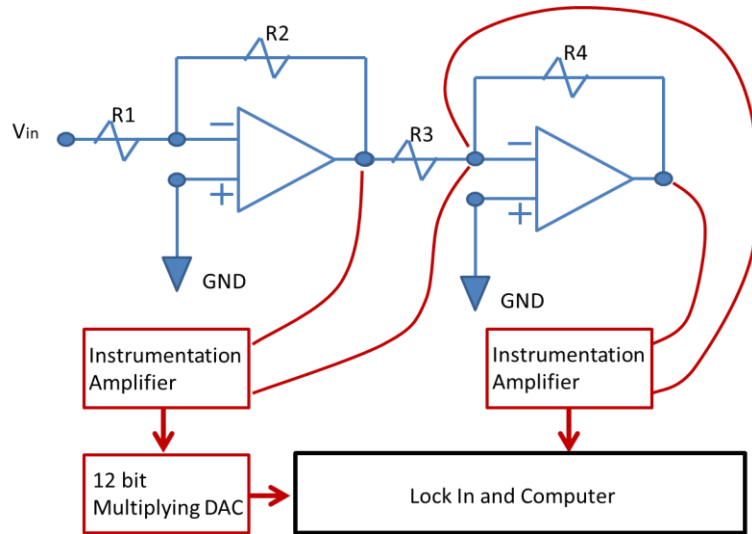


Figure 2.5: Simplified current source circuit with instrumentation amplifiers. The lock in, computer and DAC form a feedback loop to match the voltage drop across R3 and R4 read by the computer.

Instrumentation amplifiers are a buffered type of differential amplifier with the integrated chip containing five operational amplifier circuits. The output is the difference between the two inputs. A 12-bit multiplying DAC is controlled by a Labview computer program through the use of a National Instruments USB-6008 usb-powered data acquisition (DAQ) module. The 12 bit multiplying DAC paired with the USB-6008 DAQ is capable of reducing the signal by 4096 times the input value.

A custom temperature stage was fabricated to be used for the measurements, Figure 2.7. The temperature stage used a commercial thermoelectric module (Tellurex C2-55-2812) to provide cooling and heating. The temperature range of the stage ranges from 250K to 375K. The upper limit is due to the manufacturer specifications for the solder used to connect each of the thermoelectric legs. The lower limit is due to the maximum ΔT the

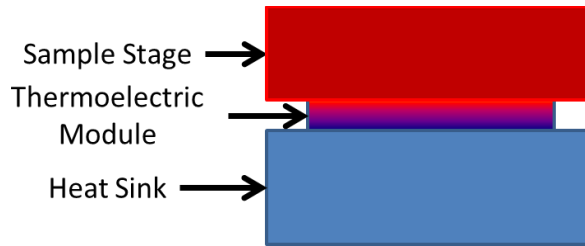


Figure 2.7: Basic layout of sample stage and heat sink relative to the thermoelectric module.

Table 2.1: Current source main components list.

Component	Manufacturer	Model	Details	
Amplifier	Texas Instruments	OPA551	OP AMP, HIGH VOLT, DIP8, 551	
Resistors	R1	Vishay Dale	PTF5650R000BYEK	METAL FILM, 50 OHM, 125mW, 0.1%
	R2	Vishay Dale	PTF5650R000BYEK	METAL FILM, 500 OHM, 125mW, 0.1%
	R3	Ohmite	45F100E	WIREWOUND, 100OHM, 5W, 1%
Capacitors	Vishay	225232500104	CERAMIC 0.1UF, 50V, X7R, 10%, RAD	
	Vishay Roederstein	MKT1813610015	POLY FILM FILM 10UF 10%, 100V	

2.3 Results

A Stanford Research Systems (SRS) model SR830 DSP lock in amplifier was used during the testing and verification of the entire system. Equation 2.3 states that the current provided to the sample is a product of the input voltage and resistors used. Resistors R1 and R2 are preset and are not interchangeable. Resistor R3, however, can be selected based on the resistance of R4. The value of R3 must be larger than R4 in order for the subtraction circuit to function properly. A resistance of 50Ω was used for R3. The performance and amplification accuracy of the circuit is presented in Figure 2.8 below. Voltage amplitudes ranging from 0.25 to 1V over a frequency range of 100 to 30,000 Hz were used. The maximum input of 1V translates to a current output of 200mA across the sample and was

selected due to the limitations of the amplifiers. 30,000 Hz was selected for the maximum frequency due to the SR830 lock-in's signal acquisition limit of 100,000 Hz.

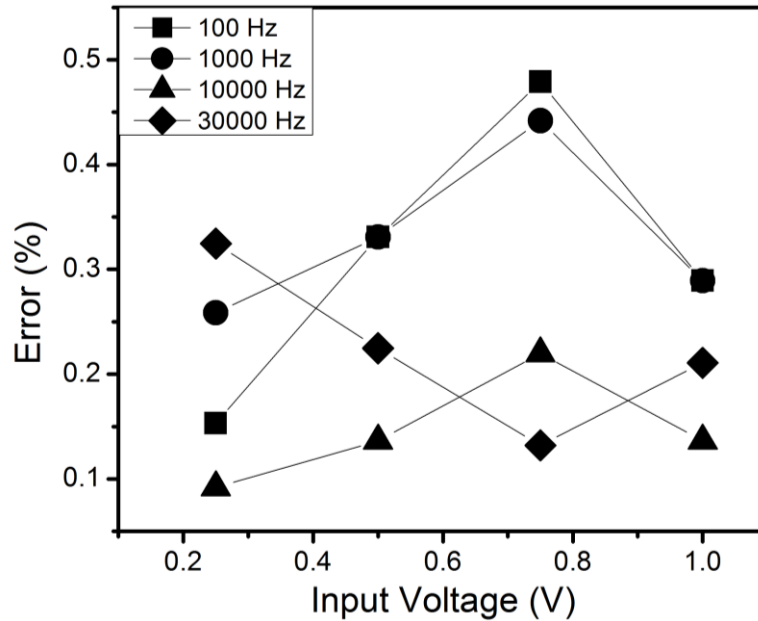


Figure 2.8: Current source voltage output error for a range of voltages and frequencies. Maximum error is 0.47% at 100 Hz with input voltage amplitude of 0.75V. There is no apparent relationship between accuracy, frequency, or input voltage.

An analysis of the third harmonic voltage generated by the circuit is also necessary. Any noise generated by the circuit will decrease the accuracy and invalidate the 3ω measurement. A larger third harmonic signal is detected at the output of the current source with increasing input voltage. This third harmonic signal fluctuates with time and only the maximum values were recorded. The SR830 lock in amplifier was used to provide the input signal to the circuit and a fluctuating third harmonic was detected from the lock in on the orders of one to the tens of microvolts.

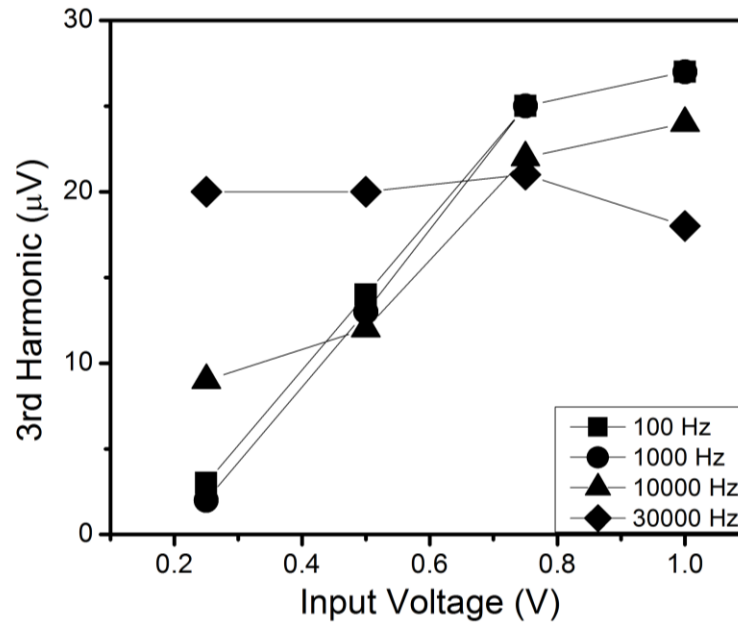


Figure 2.9: 3rd harmonic voltage output by the current source. There is an increasing trend with increasing input voltage.

The 3ω circuit produced thermal conductivity measurement values within 3% of the existing system and commercial equipment as shown in Figure 2.10. Samples of polycrystalline aluminum nitride (AlN) and alumina (Al_2O_3) were measured, both of which are optical materials. These two samples were chosen due to their differences in thermal conductivities. The AlN sample was synthesized using the current activated pressure assisted densification method in which powder is compacted to form a bulk sample. The Al_2O_3 sample was a commercially available sample.

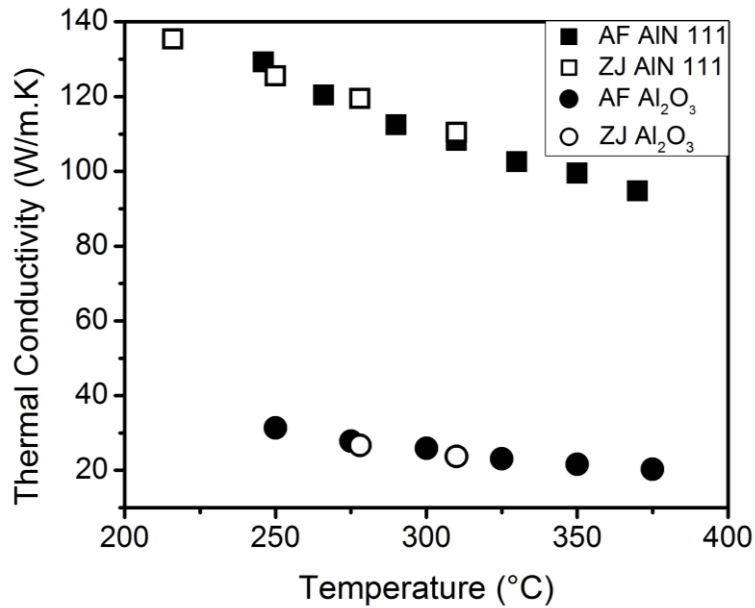


Figure 2.10: Thermal conductivity of AlN and Al₂O₃ vs Temperature. Solid shapes represent the values from the equipment built in this thesis. Outlined shapes represent the values from the previously established system.

2.4 Discussion

The development of the current source was time intensive due to the lack of literature for practical circuit design. Many issues with noise were considered anomalous until it was realized that component placement and wire routing was crucial. Longer lengths of wire can act as antennas and pick up electrical noise from radio waves. All materials have a certain amount of electrical resistance, capacitance, and inductance. Using shorter wires also decreases these three contributions. The presence of noise at ranges of frequencies and output voltages was analyzed and is considered to be within acceptable limits considering the simplicity of the circuit.

The accuracy of the 3ω measurement was reassuring due to the many factors that influence the measurement. Degradation of the heater line due to time and amount of usage

during previous measurement is an important factor when taking multiple measurements on a sample. Application of large amounts of current is capable of overheating the heater and rendering it unusable. Thermal cycling of the sample from high to low temperatures also induces strain on the small heater.

2.5 Conclusions

A low cost, high precision (<0.5%), high output (200mA) current source was produced for 3ω thermal conductivity measurements. Thermal measurements using this home build equipment are within 3% agreement with previously attained values. This close agreement provides strong evidence for the development of a practical home built 3ω thermal conductivity measurement system.

Chapter 3 Synthesis, Characterization, and Property Measurement of

Magnesium Silicide

3.1 Introduction

Magnesium silicide has been studied as a thermoelectric material since the 1950s [26–28]. Polycrystalline Mg_2Si is normally synthesized through two ways, melting or mechanical alloying the two elements together. In this work, the CAPAD technique was used to synthesize bulk samples of Mg_2Si in order to take advantage of the method's aforementioned excellent control of microstructure. The roles of CAPAD parameters on the resulting microstructure are presented. Specifically, experiments have been conducted to find the appropriate parameters to produce samples containing the necessary densities and microstructure. The majority of the experiments show the effects of processing temperature and hold time on the final density of the Mg_2Si samples. Finally, three final bulk samples were chosen for property measurement.

3.2 Experimental Procedures

3.2.1 Powder Processing

Planetary ball milling is a common technique to break down powder particulates and reduce the grain size. With this technique, jars and balls made of various hard materials such as stainless steel, agate, tungsten carbide, silicon nitride, etc, are spun around in a planetary gear fashion. The jars are located at the planetary gear positions where the rotation from the sun wheel combined with the jars produce greater acceleration than the individual gear positions. The repeated shear and impact forces between the balls and jar walls break down the particulates [29]. Main parameters include the RPM of the jars, duration, ball size, number of balls, and ball to powder ratio. A Frisch Premium Line

Pulverisette 7 planetary ball mill with stainless steel balls and jars was used for the work presented in this thesis.

The Mg_2Si starting powder was purchased from Alfa Aesar with 20 mesh size and 99.9% metals basis purity. The powder to ball weight ratio used was 1:20 and 4.7 mm diameter steel balls were used. The ball milling parameters used were 300 RPM for 6 and 12 hours and 600 RPM for 48 hours. The speed of 600 RPM for 48 hours was chosen as an extreme case to check if further powder refinement could be achieved.

3.2.2 CAPAD

The powder was consolidated inside graphite plungers and dies. Traditionally, the CAPAD uses a single die setup for producing samples with a diameter of 19mm. In this work, a specially designed mini system consisting of a small die within a larger die was used to produce samples of 9.5mm in diameter. The smaller sized samples were achieved by fabricating a smaller die and plunger set that rests inside the regular system as illustrated by Figure 3.1. This allows for less powder to be expended per sample. It is particularly useful for determining densification parameters for powders of limited supply where many experiments need to be done.

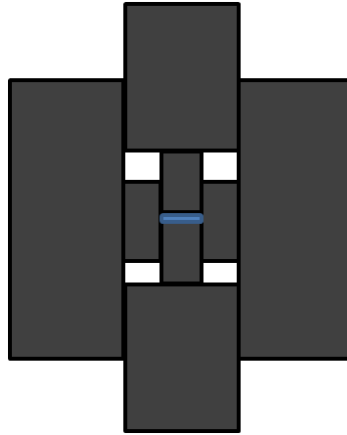


Figure 3.1: Cross section of mini die within a regular sized graphite die and plunger set.

A typical CAPAD experiment requires the application of pressure while simultaneously heating the sample. During the pressure ramp portion, very little current is supplied to the sample and dies so as to not cause excessive stress from the loading and thermal expansion. Once the desired pressure is reached, the true temperature ramp is put into effect as illustrated by Figure 3.2. The particular setup uses an Instron model 5584 testing machine. The Instron machine provides precise control over compressive forces and extension. This allows for real time densification monitoring.

The starting powders were loaded into the dies and first compacted at 112 MPa at room temperature for one minute. These green compacts were then processed at 112 MPa of pressure with a load rate of 37.3 MPa/min. The temperature ramp during this pressure ramp was held at a rate of 100 °C/min. Once the pressure stabilized at 112 MPa, the temperature ramp was increased to 200 °C/min until reaching the desired processing temperature. Two separate hold times were used, 1 and 5 minutes. These hold times began once the sample reached their processing temperatures. Densities were measured using the Archimedes method in ethanol due to the samples reactivity with water. The Archimedes

method relies on the difference in object weight due to the buoyancy force acting on a submerged object in a fluid with known properties to calculate density of the object.

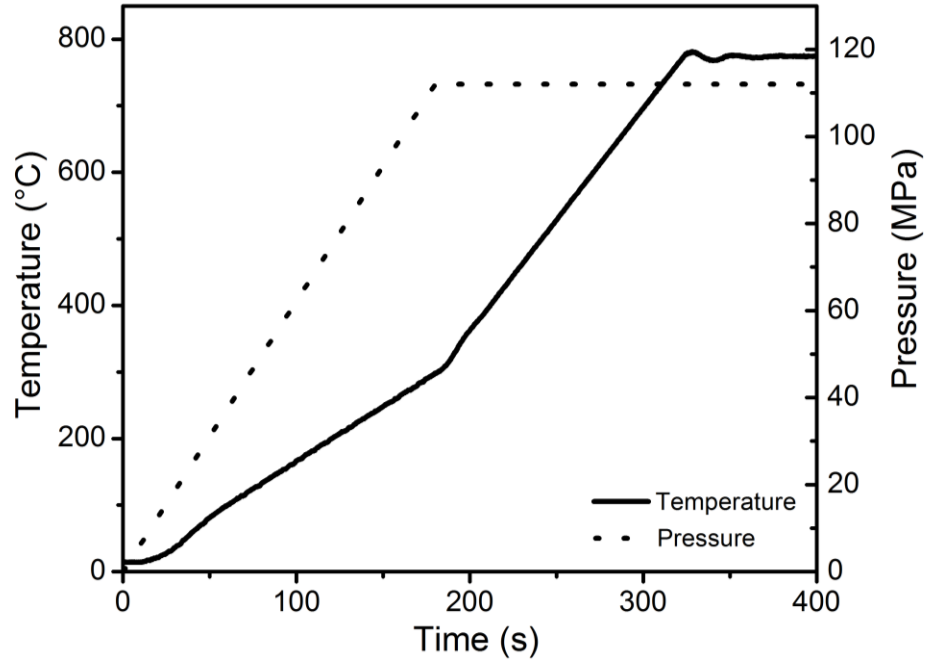


Figure 3.2: Sample CAPAD temperature and pressure curves during an experiment. The experiment lasted 400 seconds using a pressure of 112 MPa and temperature of 775 °C.

3.2.3 Microstructure Analysis

Analysis of the powder was aided through the use of a Bruker D8 Advance for x-ray diffraction (XRD) and a Philips FEG XL30 scanning electron microscope (SEM). XRD analysis provided information about both composition and microstructure. Using the Scherrer equation, crystallite size can be estimated from the XRD peak patterns [30]:

$$\chi = \frac{K\lambda}{B\sin(\theta)} \quad 3.1$$

where χ is the mean crystallite size, K is the shape factor, λ is the x-ray wavelength, B is the full width half maximum (FWHM), and θ is the Bragg angle.

The Bragg angle at which the peaks occur can also reveal information about the crystal structure. If the peak shifts are attributed towards a change in crystallographic lattice parameters, then the amount of change is calculable using Bragg's law:

$$n\lambda = 2d\sin(\theta) \quad 3.2$$

where n is an integer of a given order, λ is the wavelength of the x-ray, θ is the incident angle, and d is the plane spacing. Since Mg_2Si crystallizes in a cubic structure, the relationship between plane spacing and lattice parameter takes the form of:

$$\frac{1}{d^2} = \frac{h^2 + k^2 + l^2}{a^2} \quad 3.3$$

where h, k, l are the Miller indices and a is the lattice parameter [30].

3.2.4 Property Measurements

Electrical conductivity of the samples was measured using the home built current source described in Chapter 2. Samples were formed into bars of known dimensions and polished using a Buehler EcoMet 3000 wheel polisher and silicon carbide polishing paper with a final polish of $1\mu\text{m}$ diamond solution. An alcohol base lubricant was used. Four wires were then attached to the bars to perform a 4 point probe electrical resistivity measurement.

Seebeck coefficients of the samples were measured using the technique described by Tritt [18]. Samples were cut into bars (The bars used for electrical conductivity measurements were also used in the Seebeck coefficient measurements.) with a heater attached to one end and a heat sink on the other. A strain gauge was used as the heater to produce joule heating while an aluminum block was used as the heat sink. Thermocouples and voltage leads were placed at both ends to measure the temperature and voltage drop across the sample.

Thermal conductivity was calculated from the measured density, specific heat capacity, and measured thermal diffusivity. A custom setup was used for the measurement of thermal diffusivity in accordance with parameters outlined in ASTM C714-85. An infrared laser with 30W of effluence was used to heat the front of the sample. The sample was suspended in air by attaching a thermocouple to the backside. Convection losses were minimized by keeping the sample in an enclosed area. The 3ω method was not used due to issues with the heater line micro-fabrication. Thermal conductivity is the summation of the phonon contribution and electron contribution among other energy carriers. The relationship between electrical conductivity and electron thermal conductivity is given by the Wiedemann-Franz Law.

$$\kappa_e = \sigma LT \quad 3.4$$

where κ_e is the electron contribution to thermal conductivity, σ is the electrical conductivity, L is the Lorentz number, and T is the temperature. The Lorentz number used in the calculation was $1.5 \times 10^{-8} \text{ W/S K}^2$ for a non-degenerate semiconductor [32].

3.3 Results

The 300 RPM cycles for various lengths of time show no significant peak broadening which is caused by defects in the crystal lattice and reduction in crystallite size. Figure 3.3 shows the effect of ball milling on the 100 percent peak (220) for Mg₂Si. There is evident peak broadening with greater amounts of ball milling energy. The peaks for the ball milled powders also shift towards lower angles. Two possibilities for this shift are misalignment in the instrument and actual changes at the crystal level. The former is unlikely due to the systematic shift of ball milled powders rather than random displacements. Using equations 3.2 and 3.3, the lattice parameter can be calculated based on the XRD peak shift. The lattice parameters for the (220) peak are calculated to be 6.36 and 6.38 Å for the as received and planetary ball milled powders, respectively. These values are within 1% of the values published by Owen [31].

Table 3.1: Estimated grain size from the Scherrer equation neglecting contributions from the instrument.

RPM	Time (hrs)	Est. Grain Size (nm)
0	0	40
300	6	38
300	12	25
600	48	9

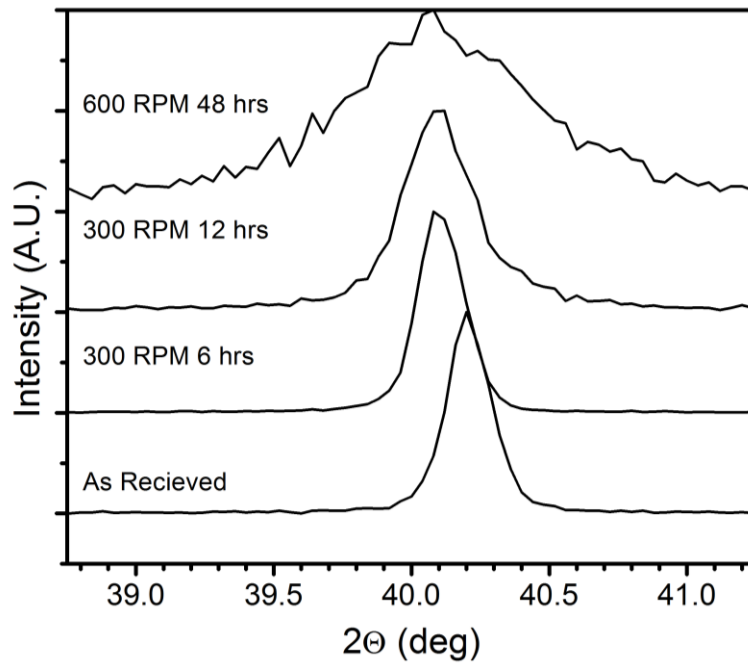


Figure 3.3: Evolution of the (220) XRD peak under different ball milling conditions. The peak shift in 2θ can be attributed towards either a change in lattice parameters or sample alignment in the instrument.

Figure 3.4 a) and b) are SEM micrographs of the powder before and after planetary ball milling at 600 RPM for 48 hours. Particulate sizes in the as received powder were in the ranges of 1-3 microns diameter. After 48 hours of planetary ball milling at 600 RPM, the powder is reduced to particulates with sizes ranging from hundreds of nanometers to 2 microns. The crystallite sizes of the powders is not readily apparent from the micrographs.

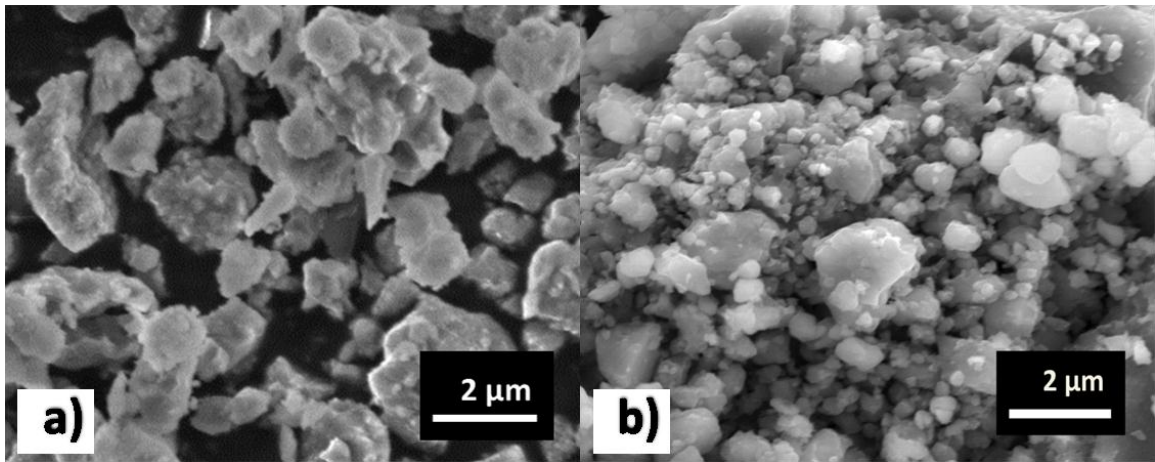


Figure 3.4: a) SEM micrograph (secondary electron) of Mg_2Si powder as received b) SEM micrograph of Mg_2Si powder ball milled at 600 RPM for 48 hours. Note the wide dispersion of particulate size.

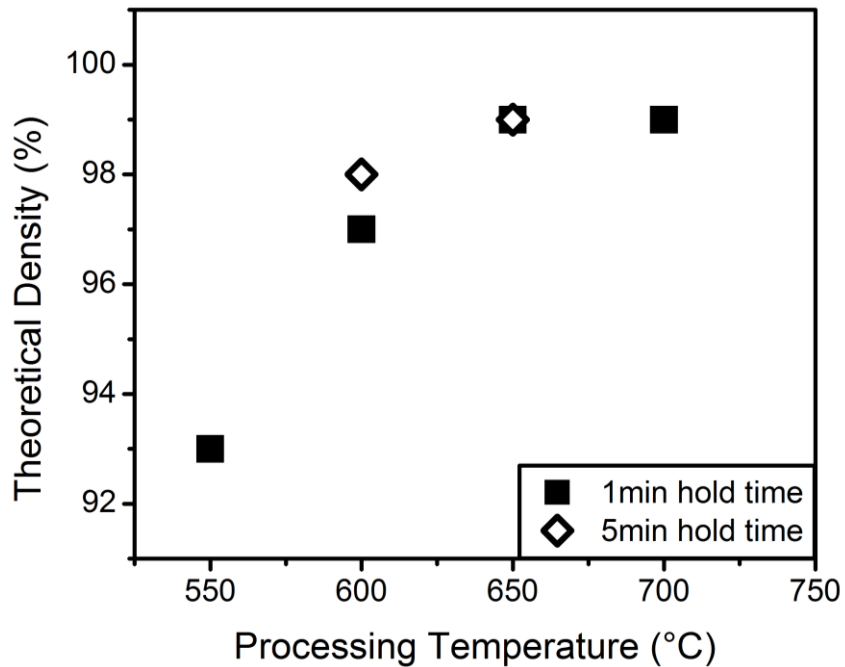


Figure 3.5: Relative densities of samples processed at varying temperatures. Regardless of hold time, a maximum density is reached for samples above 650 °C. Two samples were processed at 650 °C with densities at 99% of theoretical maximum.

Figure 3.5 shows the relative densities of samples processed at varying temperatures with uniform hold times. The powder used was planetary ball milled at 300 RPM for 6 hours. Prior to processing, the powder was compacted at room temperature with 112 MPa of pressure for one minute. The green compact densities ranged from 56-63% of the theoretical maximum.

Table 3.2: Processing parameters and corresponding densities.

Processing Temperatures [°C]	Hold Times [min]	Theoretical Densities [%]
550	1	93
600	1	97
600	5	98
650	1	99
650	5	99
700	1	99

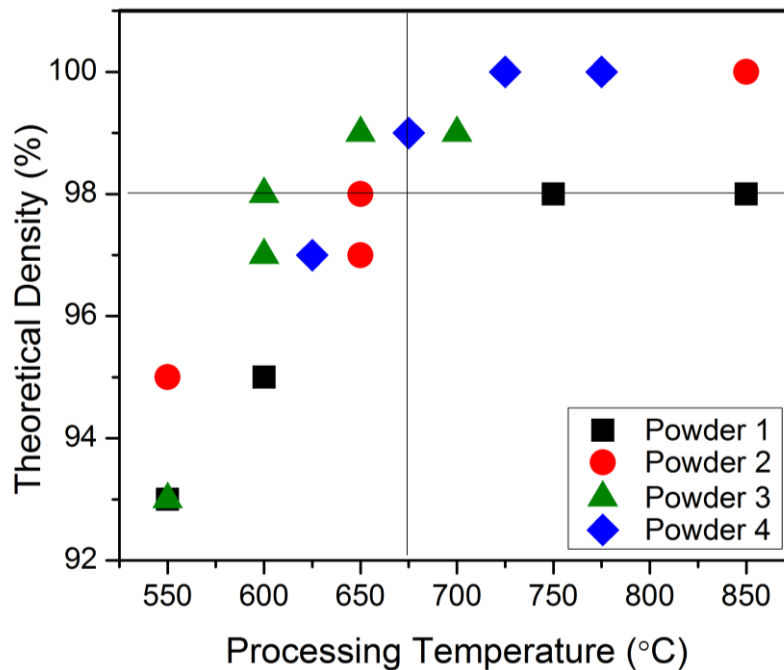


Figure 3.6: Relative densities from varying processing temperatures disregarding hold time. Four separately prepared powders were used. All powders reach their maximum density with processing temperatures above 675 °C.

Figure 3.6 shows the densities attained from densifying different powders at varying temperatures. The important relationship shown is the dependence on processing temperature. All powders reach a maximum relative density above 675 °C. This includes pre reacted powders (Powders 1, 2, 4) with varying ball milling parameters and a reaction densification powder (Powder 3). Pre-reacted powders are powders with the main phase of Mg₂Si while reaction densified powders begin as a ball milled mixture of magnesium and silicon in the stoichiometric ratio of 2:1. The diffusion which is a result of the reaction between the two powders helps drive the densification thereby reducing the processing temperature. One of the disadvantages of reaction densification is the formation of larger grains when the two powders react. Assuming a simplified reaction where two grains of powders A and B react, the resulting AB phase will be the summation of the volumes of A and B. This assumes the densities of all three phases are comparable to each other.

Table 3.3: Processing parameters and densities.

Processing Temperatures [°C]	Hold Times [min]	Densities [g/cm ³]
675	5	2.16
775	8	2.17
850	2	2.17

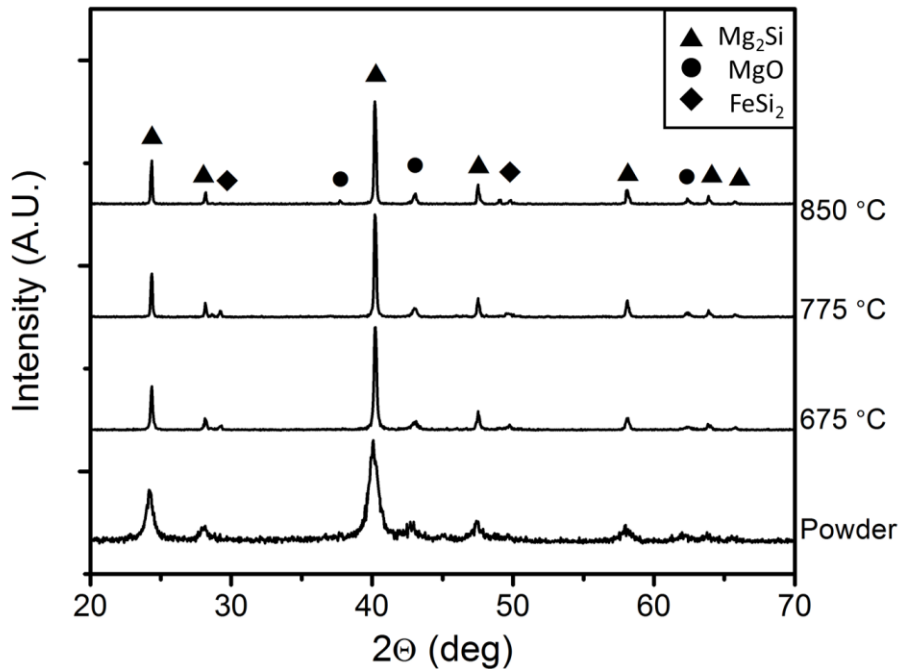


Figure 3.7: XRD curves of the ball milled powder (600RPM, 48hr) and densified samples.

Three samples were densified at temperatures of: 675, 775, and 850 °C. Their densities were measured using the Archimedes density measurement method. Figure 3.7 is a collection of XRD patterns showing which crystal phases are present in the powder and samples. There are three phases present in the densified samples: Mg₂Si, MgO, and FeSi₂. The iron impurity is from the planetary ball milling using stainless steel balls and jars. The height of the FeSi₂ peak decreases with processing temperature and is barely discernable in the sample processed at 850 °C. It is possible that FeSi₂ is not present at 850 °C due to the possibility of the iron, silicon, magnesium, and oxygen reacting to form another phase or the Fe going into solution in one of the existing phases. It is possible that the four elements form into the olivine structure, which is known to contain all four elements.

Table 3.4: Thermoelectric properties and estimated grain sizes (XRD) of samples.

Processing Temperature [°C]	Est. Grain Size [nm]	Electrical Conductivity [S/m]	Seebeck Coefficient [$\mu\text{V}/\text{K}$]	Thermal Conductivity [$\text{W}/\text{m}\cdot\text{K}$]	ZT $\times 10^3$ (300K)
675	33	5.89	537	3.11	0.164
775	38	14.41	437	4.24	0.195
850	44	31.62	350	6.29	0.185

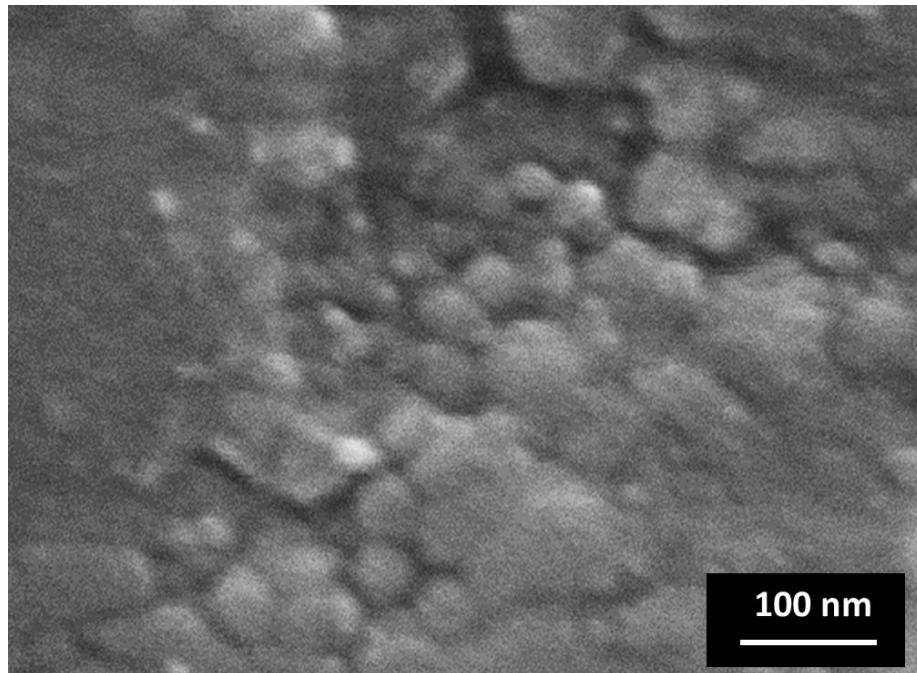


Figure 3.8: SEM micrograph (secondary electron) of the polished surface of the sample processed at 850 °C. Grains can be seen on the order of 50 nm.

Figure 3.8 is a SEM micrograph of the sample consolidated at 850 °C and demonstrates the presence of grain sizes in the range of 30 nm to 75 nm which is comparable to the sizes reported from XRD analysis. This sample was consolidated at a higher temperature than any of the other samples and therefore should have the largest grain sizes. The surface of the sample was polished using a 1 micron diamond polishing

solution. Additional attempts to image other areas on the surface of the sample were unsuccessful.

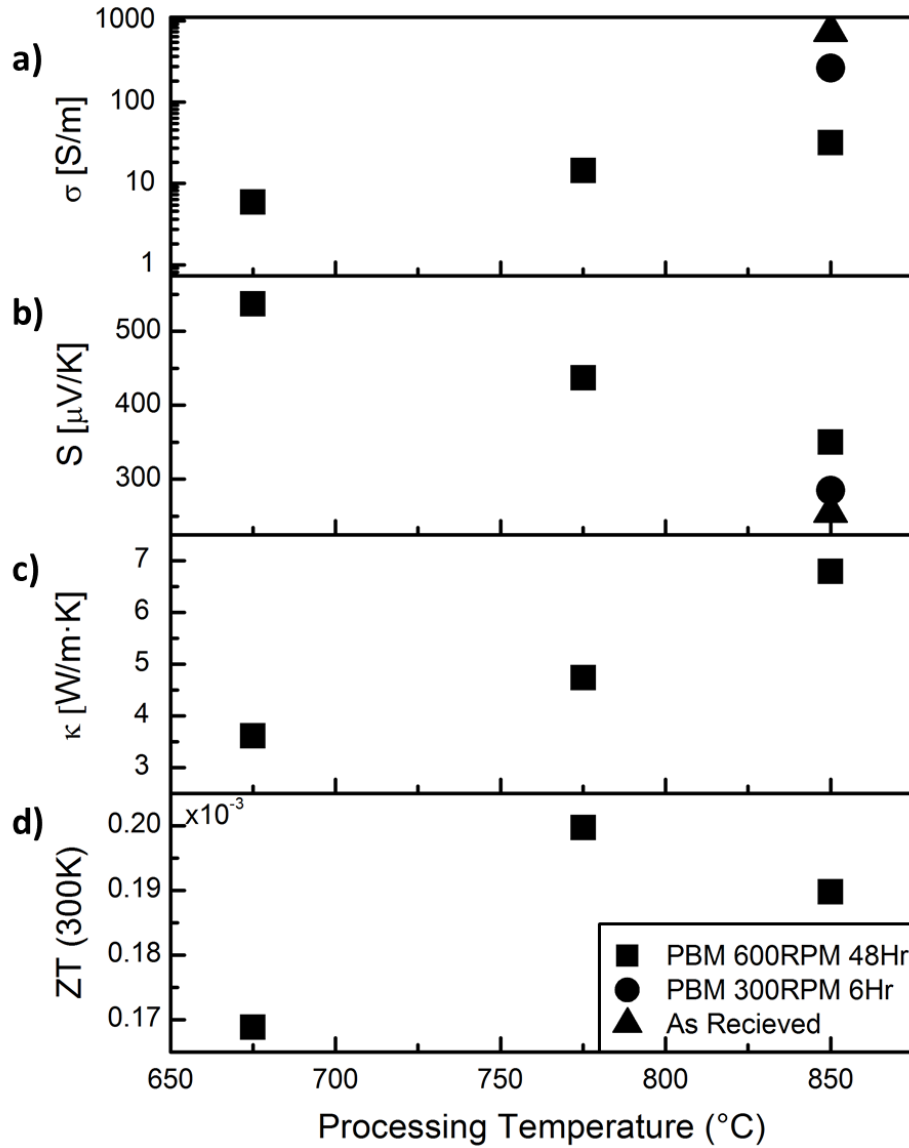


Figure 3.9: a) Electrical conductivities of samples processed at different temperatures. Higher processing temperatures result in a greater electrical conductivity. Less extensive ball milling also results in greater electrical conductivities. b) Seebeck coefficients c) Thermal conductivities and d) ZT of samples processed at different temperatures.

Figure 3.9 a) shows the electrical conductivities of five samples with five separate processing conditions. Three of the samples have the same planetary ball milling conditions but are consolidated at three separate temperatures: 675, 775, and 850 °C. The other two samples have different ball milling parameters, 300 RPM for 6 hours and none, but are processed at 850 °C. The three samples ball milled at 600 RPM for 48 hours show an increasing electrical conductivity with higher processing temperatures. This trend could either be a result of increased charge carrier mobility or an increased number of charge carriers. The other two samples show an increased electrical conductivity with a less amount of ball milling. The as received powder has the highest conductivity at 732 S/m.

Figure 3.9 b) shows the Seebeck coefficient of the same five samples mentioned previously. Increasing the processing temperature produces samples with lower Seebeck coefficients. The sample processed from the as received powder has the lowest coefficient of all five samples.

Figure 3.9 c) shows that the thermal conductivities of the samples increase with higher processing temperatures. The sample processed at 850 °C has roughly double the thermal conductivity of the sample processed at 675 °C. These values are the total contribution of phonons and electrons to the thermal conductivity. Using equation 3.4 the electron contribution can be calculated. Values are listed in Table 3.5.

Figure 3.9 d) shows the ZT value of the samples. These values are calculated using equation 1.1. The temperature used in the calculation was 300 K as all properties of the samples were measured at this temperature. The sample processed at 775 °C produced the highest figure of merit.

Table 3.5: Comparison of total thermal conductivity and the electron contribution.

Processing Temperature [°C]	Total Thermal Conductivity [W/m·K]	Electron Thermal Conductivity ($\times 10^4$) [W/m·K]
47	3.11	0.265
48	4.24	0.648
49	6.29	1.42

3.4 Discussion

Multiple bulk Mg₂Si samples were synthesized in order to attain the proper processing conditions. Since the purpose of the project is to investigate the effect of grain size on thermoelectric properties, it is important to have samples with consistent densities and compositions. Mapping of sample density with processing temperature and hold time was crucial. The amount of grain growth is highly dependent on elevated temperatures for lengths of time. The anomalous reduction of electrical conductivity compared to thermal conductivity is still being investigated. Electron mobility is severely hindered by grain boundaries [5], which is could be an explanation. Another possibility is the formation of secondary phases for the samples processed at higher temperatures. A Hall resistivity measurement is needed to ascertain the number of charge carriers present in each of the samples. Planetary ball milling provides an increased opportunity for additional contaminants and dopants to be introduced into the sample. The as received powder should ideally have the largest grain sizes and the least amount of charge carriers which supports the argument that grain size is the dominating factor in these particular samples.

Since planetary ball milling produces an inhomogeneous distribution of particulate size, XRD analysis of grain size was initially used followed by SEM. The presence of grains on the order of tens of nanometers was not realized until micrographs of grain boundaries on polished surfaces were obtained. Further analysis of the grain structure requires Transmission Electron Microscopy (TEM), which was considered to be unnecessary at first.

3.5 Conclusions

Samples with varying thermoelectric properties were successfully synthesized. Planetary ball milling reduced the grain size of the starting powder. Samples processed at lower temperatures have a reduction in both electrical and thermal conductivities while increasing the Seebeck coefficient. Currently there is evidence to relate the thermoelectric properties to a change in microstructure as measured from XRD analysis. More intensive investigation into the microstructure is still needed through TEM analysis, energy dispersive x-ray spectroscopy, and x-ray photoelectron spectroscopy.

References

- [1] N. Savvides, "Boundary scattering of phonons in fine-grained hot-pressed Ge-Si alloys. I. The dependence of lattice thermal conductivity on grain size and porosity," *Journal of Physics C: Solid State*, vol. 4657, 1980.
- [2] A. Balandin and K. Wang, "Effect of phonon confinement on the thermoelectric figure of merit of quantum wells," *Journal of applied physics*, vol. 84, no. 11, pp. 6149–6153, 1998.
- [3] C. Dames, "Theoretical phonon thermal conductivity of Si/Ge superlattice nanowires," *Journal of Applied Physics*, vol. 95, no. 2, p. 682, 2004.
- [4] M. G. Kanatzidis, "Nanostructured Thermoelectrics: The New Paradigm? †," *Chemistry of Materials*, vol. 22, no. 3, pp. 648–659, Feb. 2010.
- [5] N. Satyala and D. Vashaee, "The effect of crystallite size on thermoelectric properties of bulk nanostructured magnesium silicide (Mg₂Si) compounds," *Applied Physics Letters*, vol. 100, no. 7, p. 073107, 2012.
- [6] B. Poudel, Q. Hao, Y. Ma, Y. Lan, A. Minnich, B. Yu, X. Yan, D. Wang, A. Muto, D. Vashaee, X. Chen, J. Liu, M. S. Dresselhaus, G. Chen, and Z. Ren, "High-thermoelectric performance of nanostructured bismuth antimony telluride bulk alloys," *Science*, vol. 320, no. 5876, pp. 634–638, 2008.
- [7] M. S. Dresselhaus, G. Chen, M. Y. Tang, R. G. Yang, H. Lee, D. Z. Wang, Z. F. Ren, J.-P. Fleurial, and P. Gogna, "New Directions for Low-Dimensional Thermoelectric Materials," *Advanced Materials*, vol. 19, no. 8, pp. 1043–1053, Apr. 2007.
- [8] P. Pichanusakorn and P. Bandaru, "Nanostructured thermoelectrics," *Materials Science and Engineering: R: Reports*, vol. 67, no. 2–4, pp. 19–63, Jan. 2010.
- [9] T. Seebeck, *Magnetische polarisation der metalle und erze durch temperatur-differenz Volume 70 of Ostwalds Klassiker der exakten Wissenschaften*. W. Engelmann.
- [10] J. C. A. Peltier, "Nouvelles expériences sur la caloricité des courants électrique," *Annales de Chimie et de Physique*, vol. 56, no. 371, pp. 371–386, 1834.
- [11] C. Goupil, W. Seifert, K. Zabrocki, E. Müller, and G. J. Snyder, "Thermodynamics of Thermoelectric Phenomena and Applications," *Entropy*, vol. 13, no. 8, pp. 1481–1516, Aug. 2011.

- [12] C. Vining, D. Rowe, and J. Stockholm, "History of The International Thermoelectric Society," in *Thermoelectrics Handbook: Macro to Nano-Structured Materials*, 2005, p. AI-1-AI-9.
- [13] A. F. Joffe, "The Revival of Thermoelectricity," *Scientific American*, vol. 199, no. 5, pp. 31-37, Nov. 1958.
- [14] T. Harman, M. Walsh, and B. Laforge, "Nanostructured thermoelectric materials," *Journal of electronic materials*, vol. 34, no. 5, pp. L19-L22, May 2005.
- [15] R. Venkatasubramanian, E. Siivola, T. Colpitts, and B. O'Quinn, "Thin-film thermoelectric devices with high room-temperature figures of merit," *Nature*, vol. 413, no. 6856, pp. 597-602, Oct. 2001.
- [16] D. Cahill, "Thermal conductivity measurement from 30 to 750 K: the 3ω method," *Review of Scientific Instruments*, no. May 2008, 1990.
- [17] D. G. Cahill, "Analysis of heat flow in layered structures for time-domain thermoreflectance," *Review of Scientific Instruments*, vol. 75, no. 12, p. 5119, 2004.
- [18] T. M. Tritt, "Electrical and Thermal Transport Measurement Techniques for Evaluation of the Figure-of-Merit of Bulk Thermoelectric Materials," in *Thermoelectrics Handbook*, 2005, pp. 23-1 -23-20.
- [19] J. Martin, T. Tritt, and C. Uher, "High temperature Seebeck coefficient metrology," *Journal of Applied Physics*, vol. 108, no. 12, p. 121101, 2010.
- [20] J. E. Garay, "Current-Activated, Pressure-Assisted Densification of Materials," *Annual Review of Materials Research*, vol. 40, no. 1, pp. 445-468, Jun. 2010.
- [21] R. Coble, "Diffusion models for hot pressing with surface energy and pressure effects as driving forces," *Journal of applied physics*, vol. 41, no. 12, pp. 4798-4807, 1970.
- [22] Y.-M. Chiang, D. P. I. Birnie, and W. D. Kingery, *Physical Ceramics*. New York: John Wiley & Sons, Inc., 1997.
- [23] C. V. Thompson, "Grain Growth in Thin Films," *Annual Review of Materials Science*, vol. 20, no. 1, pp. 245-268, Aug. 1990.
- [24] H. Johnson, "Why 50 Ohms?," *EDN*, p. 30, 2000.

- [25] J. Drewniak and T. Hubing, "Modeling power bus decoupling on multilayer printed circuit boards," *IEEE Transactions on Electromagnetic Compatibility*, vol. 37, no. 2, pp. 155–166, 1995.
- [26] G. V. Raynor, *The physical metallurgy of magnesium and its alloys*. Pergamon Press, 1959.
- [27] R. G. Morris, R. D. Redin, and G. C. Danielson, "Semiconducting Properties of Mg₂Si Single Crystals," *Physical Review*, vol. 109, no. 6, pp. 1909–1915, 1958.
- [28] U. Winkler, "Electrical Properties of the Intermetallic Compounds Mg₂Si, Mg₂Ge, Mg₂Sn, Mg₂Pb," *Helv. Phys. Acta*, vol. 28, no. 633, 1955.
- [29] J. Schilz, M. Riffel, and K. Pixius, "Synthesis of thermoelectric materials by mechanical alloying in planetary ball mills," *Powder Technology*, vol. 105, no. 1–3, pp. 149–154, Nov. 1999.
- [30] B. D. Cullity and S. R. Stock, *Elements of X-ray Diffraction*, 3rd ed. Upper Saddle River: Prentice Hall, 2001.
- [31] E. Owen, "The atomic structure of two intermetallic compounds," *Proceedings of the Physical Society of*, vol. 341, 1923.
- [32] E. S. Toberer, L. L. Baranowski, and C. Dames, "Advances in Thermal Conductivity," *Annual Review of Materials Research*, vol. 42, no. 1, pp. 179–209, Aug. 2012.